arXiv:2606.04771v1 [quant-ph] 3 Jun 2026

Pushing the Classical Frontier of 1D Fermi–Hubbard Quench Dynamics Beyond Current Quantum Simulations

Roman Rausch,[1] Sukhbinder Singh,[2] Saeed S. Jahromi,[1,3]
Augustine Kshetrimayum,[1] Román Orús[1,3,4]

[1]Multiverse Computing, San Sebastián, Spain
[2]Multiverse Computing, Toronto, Ontario, Canada
[3]Donostia International Physics Center, San Sebastián, Spain
[4]Ikerbasque Foundation for Science, Bilbao, Spain

Establishing quantum advantage requires comparison against the best achievable classical simulation. The Q-CTRL team (*1*) recently simulated quench dynamics of the one-dimensional Fermi–Hubbard model on an IBM processor, completing a $L = 60$ evolution to time $t = 6$ in under three minutes and claiming a 3000× speedup over classical Time-Dependent Variational Principle (TDVP) simulation at bond dimension $\chi = 4096$. Their classical benchmark required over 160 hours on a CPU cluster, failed to converge in the high-entanglement regime $t \in [5.2, 6]$, and left the most challenging window of the experiment unverified. Here, we push the boundaries of classical simulation by exploiting the full $\mathrm{U}(1) \times \mathrm{SU}(2)$ symmetry of the Fermi–Hubbard Hamiltonian combined with GPU-accelerated tensor contractions. Reaching bond dimensions up to $\chi \approx 62{,}000$ on four NVIDIA H200 GPUs — among the largest ever achieved in

TDVP simulations and fifteen times larger than Q-CTRL's classical baseline — we achieve fully converged results across the entire simulation window, including rigorous certification of the previously unresolved high-entanglement regime $t \in [5.2, 6]$. We further advance the classical frontier to $t = 7$, which lies beyond the quantum hardware experiment and any previously verified classical evolution of the full wavefunction. At the bond dimension comparable to Q-CTRL's best classical run, our GPU implementation completes in ~ 100 minutes, directly reducing the claimed $3000\times$ quantum advantage to $\sim 36\times$. These results substantially narrow the quantum–classical performance gap and establish a new standard for tensor-network benchmarking of large-scale quantum simulations.

1 Introduction

Quantum processors have grown rapidly in scale and quality, and the field is now shifting from demonstrating that deep circuits can be run to asking whether they deliver genuine scientific value (*2, 3*). Quench dynamics of the one-dimensional Fermi–Hubbard model (FHM) has emerged as a leading testbed for this question (*1, 4*): the model supports spin-charge separation and Luttinger liquid physics, its entanglement grows rapidly under time evolution, and it maps naturally onto superconducting qubits via the Jordan–Wigner transformation (*5, 6*). Rigorous classical verification remains essential, however. Gate errors accumulate over long circuits, and without a reliable classical reference it is impossible to determine whether a quantum device faithfully tracks the true dynamics. Matrix Product State (MPS) methods, and in particular the Time-Dependent Variational Principle (*7–9*), are the leading classical tool for this purpose in one dimension, with accu-

racy controlled by the bond dimension χ. Notably, in several recent quantum advantage experiments tensor-network simulations have matched or surpassed the quantum hardware output (*10–13*), underscoring the need to deploy the most capable classical methods before any advantage claim is accepted (*14*).

The largest FHM quench simulation reported to date was performed by the Q-CTRL team (*1*), who evolved a half-filled Néel state on $L = 60$ fermionic sites (120 qubits) to time $t = 6$ using an IBM Heron superconducting processor, completing in 2 minutes 46 seconds of QPU time. For the classical benchmark they used U(1) $\times$ U(1)-symmetric TDVP at bond dimensions up to $\chi = 4096$ via the ITensor library (*15*), requiring over 160 hours on a CPU cluster. This benchmark agreed with the quantum hardware for $t \lesssim 5.2$, but diverged beyond that point, leaving the high-entanglement window $t \in [5.2, 6]$ unverified. Comparing the CPU runtime to the bare QPU time, the authors claimed a 3000$\times$ quantum speedup.

Here we push the boundaries of classical simulation to directly address this verification gap. By exploiting the full U(1)$\times$SU(2) symmetry of the half-filled FHM — going beyond the U(1) $\times$ U(1) subgroup used by Q-CTRL — combined with GPU-accelerated tensor contractions, we reach bond dimensions up to $\chi \approx 62{,}000$ on four NVIDIA H200 GPUs, among the largest ever achieved in TDVP simulations. At the bond dimension comparable to Q-CTRL's best classical run, our implementation completes in $\sim$100 minutes, directly reducing the claimed 3000$\times$ quantum speedup to $\sim$36$\times$. Scaling to larger bond dimensions, we achieve fully converged results across the entire Q-CTRL window — providing the first rigorous classical certification of the high-entanglement regime $t \in [5.2, 6]$ — and extend the simulation to $t = 7$, beyond both the reach of the quantum hardware and any previously verified classical benchmark.

2 Model and Simulation Setup

The 1D Fermi–Hubbard model is defined by the Hamiltonian

$$H = -t_h \sum_{\langle i,j\rangle,\sigma} \left(c^\dagger_{i\sigma} c_{j\sigma} + \text{h.c.} \right) + U \sum_i n_{i\uparrow} n_{i\downarrow}, \tag{1}$$

where $c^\dagger_{i\sigma}$ ($c_{i\sigma}$) creates (annihilates) a fermion of spin $\sigma \in \{\uparrow, \downarrow\}$ on site i, and $n_{i\sigma} = c^\dagger_{i\sigma} c_{i\sigma}$ is the number operator. Following Ref. (*1*), we set $t_h = 1$ as the unit of energy and consider a chain of $L = 60$ sites with open boundary conditions, matching the largest system studied in their quantum simulation.

At half-filling, the spectral properties of the FHM depend on the sign of U. For repulsive interactions ($U > 0$), a finite charge gap opens (the Mott gap), while the spin sector remains gapless, giving rise to spin-charge separation and Tomonaga–Luttinger liquid behavior. For attractive interactions ($U < 0$), we are in the Luther–Emery liquid regime where the roles are exchanged: a spin gap develops due to singlet pair formation, while the charge sector remains gapless. The Q-CTRL experiment (*1*) operates in this latter regime with $U = -2$, using 30 first-order Trotter steps of size $\Delta t = 0.2$. The quench dynamics reveal holons and spinons propagating at distinct velocities — a signature of spin-charge separation.

2.1 Symmetries: the key to acceleration

The FHM conserves total fermion number N and z-component of spin S^z, giving a $\mathrm{U}(1)_{\text{charge}} \times \mathrm{U}(1)_{\text{spin}}$ symmetry — the combination exploited by Q-CTRL (*1*). The full symmetry group, however, is larger: $\mathrm{SO}(4) \cong \mathrm{SU}(2)_{\text{spin}} \times \mathrm{SU}(2)_{\text{charge}}$, where the charge SU(2) (*16,17*) interconverts empty and doubly occupied sites. In the Q-CTRL experiment, the quantum simulation begins from the half-filled Néel state

$$|\uparrow\downarrow\uparrow\downarrow\cdots\rangle = \left(\prod_{i\in A} c^\dagger_{i\uparrow} \right) \left(\prod_{j\in B} c^\dagger_{j\downarrow} \right) |0\rangle, \tag{2}$$

where A and B denote the two sublattices. This state has total pseudospin $T_{\text{tot}} = 0$ and $S^z = 0$, but not a well-defined total spin $S_{\text{tot}} = 0$, thus breaking the full symmetry to a $\mathrm{U}(1)_{\text{spin}} \times \mathrm{SU}(2)_{\text{charge}}$ symmetry throughout the dynamics. Exploiting this symmetry (larger than $\mathrm{U}(1)_{\text{spin}} \times \mathrm{U}(1)_{\text{charge}}$ considered in (*1*)), which groups tensor indices into multiplets via the Wigner–Eckart theorem (*18–21*), reduces the effective number of independent tensor components by a factor of $\mathcal{O}(\chi^{1/3})$–$\mathcal{O}(\chi^{1/2})$ (*20–23*). Since TDVP cost scales as χ^3, this alone yields a large speedup at fixed accuracy. Technical details of the symmetry decomposition and bond-dimension taxonomy are given in the Supplementary Materials.

3 GPU-accelerated $\mathrm{U}(1) \times \mathrm{SU}(2)$-symmetric TDVP

The classical TDVP baseline in Ref. (*1*) was run using the ITensor Julia library (*15*) on an AWS `c7i.8xlarge` instance (32 vCPU, 64 GB RAM), employing $\mathrm{U}(1) \times \mathrm{U}(1)$ symmetry. At bond dimension $\chi = 4096$, this required over 160 hours to reach $t = 6$. The claimed $3000\times$ quantum advantage was obtained by comparing this runtime to the $\approx$166 seconds of bare QPU execution time, excluding readout error mitigation, decay recovery, circuit compilation, and post-processing. Our implementation improves upon this baseline on three fronts; full algorithmic details are provided in the Supplementary Materials.

Symmetry. Encoding the $\mathrm{U}(1)_{\text{spin}} \times \mathrm{SU}(2)_{\text{charge}}$ symmetry — absent in the ITensor baseline — into the MPS tensors via the Wigner–Eckart theorem (*19–23*) groups all $2T + 1$ components of each pseudospin-T multiplet into a single reduced matrix element. In practice we find $\chi \approx 2.4\,\chi_{\mathrm{SU}(2)}$, so the computational cost scales with the smaller $\chi_{\mathrm{SU}(2)}$ while the expressive power matches χ.

GPU acceleration. We implemented the algorithm in PyTorch (*24*), exploiting GPU GEMM throughput for the dominant environment-update and Krylov-exponentiation

steps. To preserve arithmetic intensity from the block-diagonal symmetry structure — a known challenge for GPU-accelerated symmetric tensor networks (*25*) — tensors of equal block size are dispatched as batched-GEMM calls. At large bond dimensions, memory becomes the binding constraint; we use `float32` arithmetic, validated against `float64` runs (see SM). For our largest simulations ($\chi \approx 62{,}000$) we distribute batched matrix multiplications across four H200 GPUs using a greedy load-balancing scheme, with SVDs performed on the CPU.

Adaptive 1-site/2-site switching. We begin with 2-site TDVP updates to allow the bond dimension to grow freely, then switch to 1-site updates once it saturates, eliminating per-step SVD overhead entirely. This yields a 4–10× wall-clock speedup for the later time steps relative to 2-site updates throughout, as used by Q-CTRL. The SVD truncation threshold $\epsilon_{\text{tol}} = 10^{-4}$ — looser than the 10^{-8} used by Q-CTRL — delays bond-dimension saturation and reduces average cost per step while delivering converged observables; an error analysis is given in the Supplementary Materials.

4 Results

4.1 Convergence and verification of $t \in [5.2, 6]$ regime

Figure 1(a) shows the TDVP time evolution of $\langle n_{46\uparrow} \rangle$ for $L = 60$ fermions up to $t = 8$ (converged until $t = 7$, see Sec. 4.4) at truncation threshold $\epsilon_{\text{tol}} = 10^{-4}$. Our U(1) × U(1) result at $\chi = 4096$ reproduces the Q-CTRL iTensor calculation, confirming that TDVP at this bond dimension fails to converge beyond $t \approx 5$. By contrast, our U(1) × SU(2) simulation at $\chi \approx 30{,}000$ achieves convergence throughout the high-entanglement window $t \in [5.2, 6]$ (shaded blue). Figure 1(b) shows the absolute deviation from the $\chi \approx 62{,}000$ reference; it falls below 0.01 at $\chi \approx 20{,}000$ for all $t \leq 6$. Figure 1(c) shows the RMSE (see SM for definition) between our TDVP expectation values and the Q-CTRL quantum

Table 1: Wall-clock runtime to $t = 6$ at $\epsilon_{\text{tol}} = 10^{-4}$. The Q-CTRL QPU entry gives bare processor time. Full runtimes across all tolerances are in Table S1.

Implementation	χ	N_{GPU}	Runtime
Q-CTRL QPU (*1*)	—	—	2 m 46 s
Q-CTRL ITensor U(1)×U(1) (*1*)	4 096	32 vCPU	>160 h
This work with U(1)×U(1), fp64	4 096	1	3 h 27 m
This work with U(1)×SU(2), fp32	4 880	1	1 h 40 m
This work with U(1)×SU(2), fp32	30 000	1	4 h 06 m
This work with U(1)×SU(2), fp32	62 000	4	5 h 21 m

hardware data for three representative sites. The RMSE diverges at $\chi \approx 4{,}880$ but remains small for $\chi > 10{,}000$ throughout $t \in [0, 6]$, providing rigorous classical certification of the entire Q-CTRL window including the previously unresolved high-entanglement regime.

4.2 Wall-time performance and revised quantum advantage

Figure 1(d) and Table 1 compare runtimes. At $\chi = 4096$, the Q-CTRL ITensor simulation on 32 vCPUs requires over 160 h; our GPU-accelerated $\mathrm{U}(1) \times \mathrm{U}(1)$ implementation at the same bond dimension completes in ≈ 200 min. Switching to $\mathrm{U}(1) \times \mathrm{SU}(2)$ symmetry at comparable expressive power ($\chi \approx 4{,}880$) reduces this to ≈ 100 min — a $\sim 100\times$ speedup over the ITensor CPU baseline and, when compared against the QPU time of 166 s, a revised quantum advantage of $\sim 36\times$ rather than the claimed $3000\times$. Full runtimes across all bond dimensions and tolerances are given in Table S1 of the Supplementary Materials.

4.3 Full spatiotemporal benchmark

Figure 2 shows the site-resolved up-spin density $\langle n_{i\uparrow} \rangle$ computed with our $\mathrm{U}(1) \times \mathrm{SU}(2)$ TDVP at $\chi \approx 62{,}000$ (`float32`). This constitutes a converged classical benchmark for the full spatiotemporal density profile of Ref. (*1*) (Fig. 3 therein), and extends it to $t = 7$.

For comparison, the U(1) × U(1) result at $\chi = 4096$ (Fig. S4) diverges visibly at late times, confirming that a larger bond dimension is essential. Results at $t \leq 6$ are already converged at $\chi \approx 30{,}000$ (`float32`), see Fig. S5.

4.4 Extension to $t = 7$, beyond the quantum hardware

Figure 1(a) also shows results for $t \in [6, 7]$ (shaded green), a window beyond both the Q-CTRL quantum simulation and any previously verified classical benchmark. The TDVP converges in the range $\chi \approx 40{,}000$–$62{,}000$; a shallow minimum around $t \approx 6.4$ is cleanly resolved. Beyond $t = 7$, bond-dimension spread grows and we do not certify the dynamics in that regime.

5 Conclusions

We have advanced the classical benchmark for the Q-CTRL Fermi–Hubbard quench simulation (*1*) on four fronts. First, we certify the quantum simulation across the full window $t \in [0, 6]$, including the high-entanglement regime $t \in [5.2, 6]$ that the Q-CTRL classical benchmarks could not resolve. Second, our U(1) × SU(2) GPU implementation at comparable bond dimension ($\chi \approx 4{,}880$) completes in ≈100 minutes — a ∼100× speedup over the ITensor CPU baseline — which directly revises the claimed 3000× quantum advantage down to ∼36× when compared against the bare QPU time, and calls for a reassessment of that figure. Third, at $\chi \approx 62{,}000$ — among the largest TDVP bond dimensions achieved to date — we provide the first converged spatiotemporal reference for the full $L = 60$ density heatmap. Fourth, we extend the classical frontier to $t = 7$, beyond the reach of the quantum hardware itself. Taken together, these results show that combining symmetry exploitation, GPU acceleration, and adaptive truncation substantially pushes the classical simulability frontier.

The timings reported here are for full wavefunction evolution. Observable-specific methods — such as Majorana propagation (*26*) or Heisenberg-picture operator evolution — can in principle extend the simulated timescale further for particular observables of interest, and our symmetry and hardware optimizations apply equally to operator evolution.

Further progress is likely on both hardware and algorithmic fronts. Larger GPU clusters and more efficient GPU-adapted algorithms (*27–30*) will reduce runtimes at fixed bond dimension, while algorithms based on variational compression (*31, 32*) or global subspace expansion (*33, 34*) may achieve more faithful approximations at the same χ. The classical frontier for Fermi–Hubbard dynamics has moved — the question is how much further it can go.

Acknowledgments

We thank Matthias Peschke for discussions as well as Multiverse Computing for support and computational resources.

Author contributions: R.O. and S.S.J. conceived and directed the project. R.R. and S.S. developed the algorithm; R.R. implemented it in PyTorch and performed the numerical experiments. R.R., S.S., S.S.J., and A.K. designed the experiments and analysed the data. All authors contributed to writing the manuscript.

Competing interests: The authors declare no competing interests.

Data, code and materials availability: Data, code and materials availability: The data and other materials used in this study are available from the corresponding author upon reasonable request, subject to institutional and commercial constraints.

References

1. G. S. Hartnett, *et al.*, Quantum simulation of 1D Fermi-Hubbard model using a quantum computer (2025), https://arxiv.org/abs/2605.04025, arXiv:2605.04025v1.

2. J. Preskill, Quantum Computing in the NISQ era and beyond. *Quantum* **2**, 79 (2018), doi:10.22331/q-2018-08-06-79, https://doi.org/10.22331/q-2018-08-06-79.

3. A. J. Daley, *et al.*, Practical quantum advantage in quantum simulation. *Nature* **607**, 667–676 (2022), doi:10.1038/s41586-022-04940-6.

4. T. A. Chowdhury, V. Korepin, V. R. Pascuzzi, K. Yu, Quantum utility in simulating the real-time dynamics of the Fermi–Hubbard model using superconducting quantum computers. *Applied Physics Reviews* **13** (1), 011434 (2026), doi:10.1063/5.0306069, https://doi.org/10.1063/5.0306069.

5. C. Cade, L. Mineh, A. Montanaro, S. Stanisic, Strategies for solving the Fermi-Hubbard model on near-term quantum computers. *Phys. Rev. B* **102**, 235122 (2020), doi:10.1103/PhysRevB.102.235122.

6. S. Stanisic, *et al.*, Observing ground-state properties of the Fermi-Hubbard model using a programmable quantum computer. *Nature Communications* **13**, 5743 (2022), doi:10.1038/s41467-022-33335-4.

7. J. Haegeman, *et al.*, Time-Dependent Variational Principle for Quantum Lattices. *Phys. Rev. Lett.* **107**, 070601 (2011), doi:10.1103/PhysRevLett.107.070601, https://link.aps.org/doi/10.1103/PhysRevLett.107.070601.

8. J. Haegeman, C. Lubich, I. Oseledets, B. Vandereycken, F. Verstraete, Unifying time evolution and optimization with matrix product states. *Phys. Rev. B* **94**,

165116 (2016), doi:10.1103/PhysRevB.94.165116, https://link.aps.org/doi/10.1103/PhysRevB.94.165116.

9. S. Paeckel, *et al.*, Time-evolution methods for matrix-product states. *Annals of Physics* **411**, 167998 (2019), doi:10.1016/j.aop.2019.167998.

10. J. Tindall, M. Fishman, E. M. Stoudenmire, D. Sels, Efficient Tensor Network Simulation of IBM's Eagle Kicked Ising Experiment. *PRX Quantum* **5**, 010308 (2024), doi:10.1103/PRXQuantum.5.010308, https://link.aps.org/doi/10.1103/PRXQuantum.5.010308.

11. S. Patra, S. S. Jahromi, S. Singh, R. Orús, Efficient tensor network simulation of IBM's largest quantum processors. *Phys. Rev. Res.* **6**, 013326 (2024), doi:10.1103/PhysRevResearch.6.013326, https://link.aps.org/doi/10.1103/PhysRevResearch.6.013326.

12. H.-J. Liao, K. Wang, Z.-S. Zhou, P. Zhang, T. Xiang, Simulation of IBM's kicked Ising experiment with Projected Entangled Pair Operator. *arXiv e-prints* arXiv:2308.03082 (2023), doi:10.48550/arXiv.2308.03082.

13. J. Tindall, A. F. Mello, M. Fishman, E. M. Stoudenmire, D. Sels, Dynamics of disordered quantum systems with two- and three-dimensional tensor networks. *Science* **392** (6800), 868–872 (2026), doi:10.1126/science.adx2728, https://www.science.org/doi/abs/10.1126/science.adx2728.

14. A. Kshetrimayum, S. S. Jahromi, S. Singh, R. Orús, Quantum Advantage: a Tensor Network Perspective. *arXiv e-prints* arXiv:2603.18825 (2026), doi:10.48550/arXiv.2603.18825.

15. M. Fishman, S. R. White, E. M. Stoudenmire, The ITensor software library for tensor network calculations. *SciPost Phys. Codebases* p. 4 (2022), doi:10.21468/SciPostPhysCodeb.4, https://scipost.org/SciPostPhysCodeb.4.

16. P. W. Anderson, Random-Phase Approximation in the Theory of Superconductivity. *Physical Review* **112** (6), 1900–1916 (1958), doi:10.1103/PhysRev.112.1900.

17. S.-C. Zhang, Pseudospin symmetry and new collective modes of the Hubbard model. *Physical Review Letters* **65** (1), 120–122 (1990), doi:10.1103/PhysRevLett.65.120.

18. S. Singh, R. N. C. Pfeifer, G. Vidal, Tensor network decompositions in the presence of a global symmetry. *Phys. Rev. A* **82**, 050301(R) (2010), doi:10.1103/PhysRevA.82.050301, https://link.aps.org/doi/10.1103/PhysRevA.82.050301.

19. S. Singh, R. N. C. Pfeifer, G. Vidal, Tensor network states and algorithms in the presence of a global U(1) symmetry. *Phys. Rev. B* **83**, 115125 (2011), doi:10.1103/PhysRevB.83.115125, https://link.aps.org/doi/10.1103/PhysRevB.83.115125.

20. S. Singh, G. Vidal, Tensor network states and algorithms in the presence of a global SU(2) symmetry. *Phys. Rev. B* **86**, 195114 (2012), doi:10.1103/PhysRevB.86.195114, https://link.aps.org/doi/10.1103/PhysRevB.86.195114.

21. P. Schmoll, S. Singh, M. Rizzi, R. Orús, A programming guide for tensor networks with global SU(2) symmetry. *Annals of Physics* **419**, 168232 (2020), doi:https://doi.org/10.1016/j.aop.2020.168232, https://www.sciencedirect.com/science/article/pii/S0003491620301664.

22. I. P. McCulloch, From density-matrix renormalization group to matrix product states. *J. Stat. Mech.: Theory Exp.* **2007**, P10014 (2007), doi:10.1088/1742-5468/2007/10/P10014.

23. A. Weichselbaum, Non-abelian symmetries in tensor networks: A quantum symmetry space approach. *Annals of Physics* **327** (12), 2972–3047 (2012), doi:https://doi.org/10.1016/j.aop.2012.07.009, https://www.sciencedirect.com/science/article/pii/S0003491612001121.

24. R. Rausch, S. Singh, Symmetric Tensor Networks on GPUs (2026), manuscript in preparation.

25. ITensor Developers, Running on GPUs—ITensors.jl documentation (2025), https://itensor.github.io/ITensors.jl/dev/RunningOnGPUs.html, accessed: May 25, 2026.

26. A. Miller, *et al.*, Simulation of Fermionic circuits using Majorana Propagation (2025), https://arxiv.org/abs/2503.18939.

27. A. Menczer, O. Legeza, Massively Parallel Tensor Network State Algorithms on Hybrid CPU-GPU Based Architectures. *Journal of Chemical Theory and Computation* **21**, 1572–1587 (2025), doi:https://doi.org/10.1021/acs.jctc.4c00661.

28. A. Menczer, O. Legeza, Boosting the effective performance of massively parallel tensor network state algorithms on hybrid CPU-GPU based architectures via non-Abelian symmetries (2023), https://arxiv.org/abs/2309.16724.

29. A. Menczer, *et al.*, Parallel Implementation of the Density Matrix Renormalization Group Method Achieving a Quarter petaFLOPS Performance on a Single DGX-H100 GPU Node. *Journal of Chemical Theory and Computation* **20** (19), 8397–8404 (2024), doi:10.1021/acs.jctc.4c00903, https://doi.org/10.1021/acs.jctc.4c00903.

30. F. Pan, H. Gu, P. Springer, X. Li, Parallelizing Large-Scale Tensor Network Contraction on Multiple GPUs (2026), https://arxiv.org/abs/2606.01852.

31. U. Schollwöck, The density-matrix renormalization group in the age of matrix product states. *Annals of Physics* **326** (1), 96–192 (2011), doi:https://doi.org/10.1016/j.aop.2010.09.012, https://www.sciencedirect.com/science/article/pii/S0003491610001752.

32. M. Van Damme, L. Vanderstraeten, J. Haegeman, F. Verstraete, Tangent-space methods for truncating uniform matrix product states. *SciPost Phys. Core* **4**, 004 (2021), doi:10.21468/SciPostPhysCore.4.1.004.

33. M. Yang, S. R. White, Time-dependent variational principle with ancillary Krylov subspace. *Phys. Rev. B* **102**, 094315 (2020), doi:10.1103/PhysRevB.102.094315.

34. A. J. Dunnett, A. W. Chin, Efficient bond-adaptive approach for finite-temperature open quantum dynamics using the one-site time-dependent variational principle for matrix product states. *Phys. Rev. B* **104**, 214302 (2021), doi:10.1103/PhysRevB.104.214302.

35. C. Lubich, *From Quantum to Classical Molecular Dynamics: Reduced Models and Numerical Analysis*, Zurich Lectures in Advanced Mathematics (European Mathematical Society (EMS), Zürich) (2008), doi:10.4171/067.

36. P. Calabrese, J. Cardy, Evolution of entanglement entropy in one-dimensional systems. *J. Stat. Mech.: Theory Exp.* **2005**, P04010 (2005), doi:10.1088/1742-5468/2005/04/P04010.

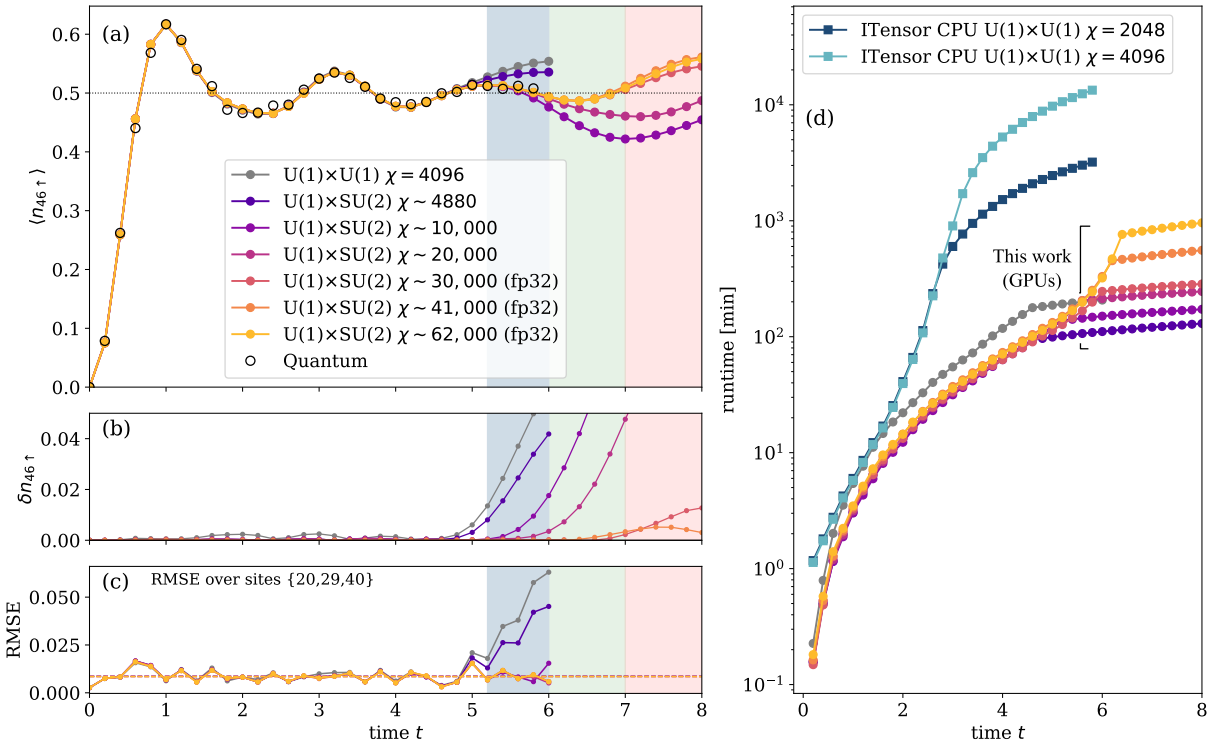

Figure 1: Main results. (a) TDVP time evolution of $\langle n_{46\uparrow} \rangle$ up to $t = 8$ for $L = 60$ fermions with $\epsilon_{\text{tol}} = 10^{-4}$. Our U(1)×U(1) curve at $\chi = 4096$ reproduces the Q-CTRL iTensor calculation and confirms non-convergence beyond $t \approx 5$. Our U(1)×SU(2) TDVP with $\chi \approx 30{,}000$ achieves convergence in $t \in [5.2, 6]$ (shaded blue) and our results are reliable in $t \in [6, 7]$ (shaded green), extending beyond the quantum simulation window. (b) Absolute deviation of $\langle n_{46\uparrow} \rangle$ from the $\chi \approx 62{,}000$ reference at each bond dimension. (c) RMSE of our TDVP data against Q-CTRL's published values of $\langle n_{20\uparrow} \rangle$, $\langle n_{29\uparrow} \rangle$, and $\langle n_{40\uparrow} \rangle$. (d) Wall-clock runtimes: ITensor TDVP on CPU cluster (*1*) vs. our GPU implementation (same legend as (a)).

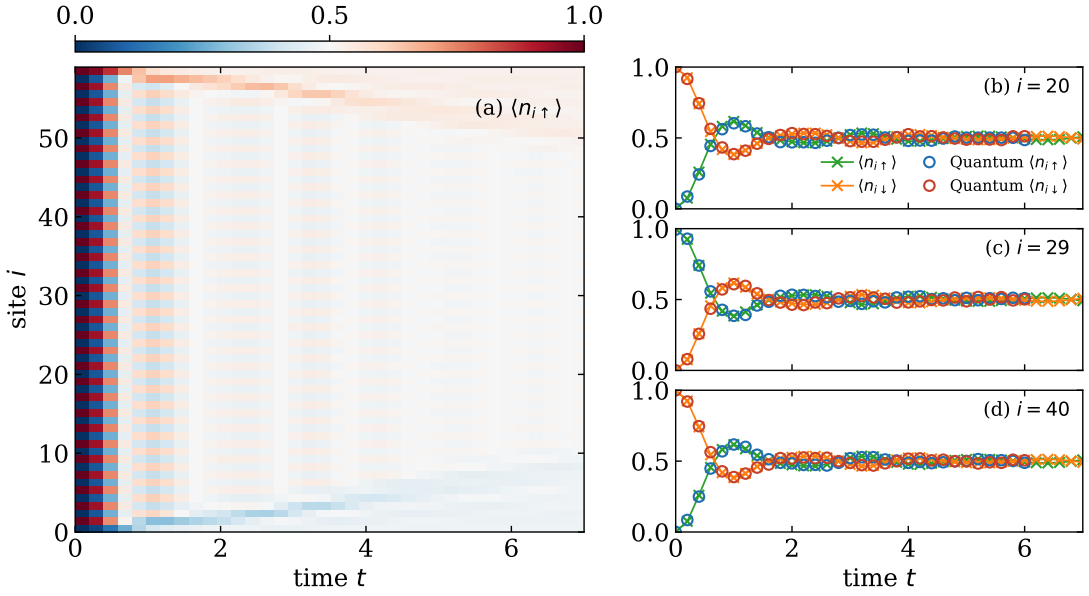

Figure 2: Classical benchmarks for the Q-CTRL quantum simulation results of Fig. 3 in Ref. (*1*). (a) Expectation value $\langle n_{i\uparrow}\rangle$ (up-spin density at site i) as a function of evolution time t, computed with our U(1) × SU(2) TDVP at $\chi \approx 62{,}000$ (`float32`, $\epsilon_{\text{tol}} = 10^{-4}$). Results already converged for $t \leq 6$ using $\chi = 30,000$ (Fig S5). (b)–(d) Site-resolved values at $i = 20$, 29, 40 compared directly with the Q-CTRL quantum simulation results.

Supplementary Materials

Pushing the Classical Frontier of 1D Fermi–Hubbard Quench Dynamics Beyond Current Quantum Simulations

Roman Rausch,[1] Sukhbinder Singh,[2] Saeed S. Jahromi,[1,3] Augustine Kshetrimayum,[1]

Román Orús[1,3,4]

[1]Multiverse Computing, San Sebastián, Spain
[2]Multiverse Computing, Toronto, Ontario, Canada
[3]Donostia International Physics Center, San Sebastián, Spain

[4]Ikerbasque Foundation for Science, Bilbao, Spain

S1 The Q-CTRL classical benchmark details

The Q-CTRL team's primary experiment reports the quench dynamics of the 1D FHM with attractive coupling $U = -2$, evolving from two initial states: a half-filled Néel state for $L = 60$ sites, Eq. 2, and a Néel state with a single central vacancy for $L = 31$ sites. The time evolution reaches $t = 6$ via 30 first-order Trotter steps of size $\Delta t = 0.2$, implemented as a circuit of 9,057 two-qubit gates at depth 152. The site-resolved spin-up occupations $\langle n_{i\uparrow}\rangle$ measured by the quantum hardware reveal clear signatures of spin–charge separation in the vacancy experiment: spinon and holon excitations propagate at distinct velocities, consistent with Luttinger liquid theory.

As a classical benchmark, TDVP simulations with U(1) × U(1) symmetry were performed at bond dimensions $\chi \in \{64, 128, 256, 512, 1024, 4096\}$ using the ITensor library (*15*). Quantum–classical agreement was quantified by the root-mean-square error (RMSE) over all $2L = 120$ spin orbitals,

$$\mathrm{RMSE} = \left(\frac{1}{2L} \sum_{i,\sigma} \Big(\langle n_{i\sigma} \rangle_{\mathrm{QC}} - \langle n_{i\sigma} \rangle_{\mathrm{TDVP}} \Big)^2 \right)^{1/2} . \tag{3}$$

The RMSE remains small for $t \lesssim 5.2$ but grows rapidly at later times even at $\chi = 4096$, indicating that this bond dimension is insufficient to resolve the dynamics in the high-entanglement regime. Pauli path propagation (PPP) was also evaluated as a second classical baseline and similarly failed to track the quantum evolution at late times. On the computational side, TDVP at $\chi = 4096$ required over 160 hours of wall-clock time to reach $t = 6$, while the quantum hardware completed the full simulation — including readout error mitigation and decay recovery — in $\approx$ 4min 25s; this figure excludes circuit compilation, data retrieval from IBM Cloud, and post-processing.

S2 Materials and Methods

S2.1 Exploiting the full $\mathrm{U}(1) \times \mathrm{SU}(2)$ symmetry

The FHM possesses exact symmetries whose exploitation is central to our simulation strategy. For any U, the total fermion number $N = N_\uparrow + N_\downarrow$ and the z-component of total spin $S^z = \frac{1}{2}(N_\uparrow - N_\downarrow)$ are separately conserved, giving a $\mathrm{U}(1)_{\mathrm{charge}} \times \mathrm{U}(1)_{\mathrm{spin}}$ symmetry — the combination used in the Q-CTRL classical benchmark (*1*). However, each U(1) is embedded in a larger SU(2), and the full symmetry group is $\mathrm{SO}(4) \cong \mathrm{SU}(2)_{\mathrm{spin}} \times \mathrm{SU}(2)_{\mathrm{charge}}$. The spin SU(2) is generated by the total spin operators $S^\pm$ and S^z. The charge SU(2) (*16, 17*) — not exploited in Ref. (*1*) — is generated by the pseudospin operators

$$T^+ = \sum_{i=1}^{L} (-1)^i \, c^\dagger_{i\uparrow} c^\dagger_{i\downarrow}, \; T^- = \left(T^+\right)^\dagger, \; T^z = \frac{N - L}{2}, \tag{4}$$

which interconvert empty and doubly occupied sites and satisfy the SU(2) algebra

$$\left[T^+, \, T^-\right] = 2T^z, \qquad \left[T^z, \, T^\pm\right] = \pm T^\pm. \tag{5}$$

These operators commute with H,

$$\left[H, \, T^\pm\right] = 0, \qquad [H, \, T^z] = 0, \tag{6}$$

and are therefore conserved throughout the time evolution. The alternating phase $(-1)^i$ in $T^{\pm}$ requires a bipartite lattice, which is satisfied by the open chain studied here.

The quantum simulation begins from the half-filled Néel state, which lies in the $S^z = 0$, $T_{\text{tot}} = 0$[1] sector, but does not have a well-defined total spin $S_{\text{tot}} = 0$. Both quantum numbers $S^z = 0$, $T_{\text{tot}} = 0$ are conserved under time evolution by H. Exploiting the resulting $\mathrm{U}(1)_{\text{spin}} \times \mathrm{SU}(2)_{\text{charge}}$ symmetry is the key ingredient that accelerates our TDVP simulation beyond the Q-CTRL benchmark.[2]

Under the action of the $\mathrm{U}(1) \times \mathrm{SU}(2)$ symmetry each MPS bond space $\mathbb{V}^{[i]}$ (Eq. 11) decomposes as

$$\mathbb{V}^{[i]} = \bigoplus_{n,j} \mathbb{D}^{[i]}_{n,j} \otimes \mathbb{V}^{[i]}_{n,j}, \tag{7}$$

where $\mathbb{V}_{n,j}$ is the $(2j+1)$-dimensional irrep labeled by particle number n and spin j, and $\mathbb{D}_{n,j}$ is the degeneracy space of dimension $d_{n,j}$.[3] As a concrete example, Table S2 lists the sector degeneracies at $t = 6$ for our $\chi_{\mathrm{SU}(2)} = 12{,}288$ ($\chi \approx 30{,}000$) simulation.

The decomposition Eq. 7 gives rise to three bond-dimension parameters:

$$\chi = \sum_{n,j} d_{n,j}(2j+1), \tag{8}$$

$$d^{\max}_{\mathrm{SU}(2)} = \max_{n,j} d_{n,j}, \tag{9}$$

$$\chi_{\mathrm{SU}(2)} = \sum_{n,j} d_{n,j}. \tag{10}$$

The *effective* bond dimension χ is the total dimension of the bond space, directly comparable to the bond dimension of the same MPS in a non-symmetric basis. The *total*

[1] T_{tot} is the total pseudospin quantum number, defined via the Casimir $(T^x)^2 + (T^y)^2 + (T^z)^2 = T_{\text{tot}}(T_{\text{tot}}+1)$, where $T^{\pm} = T^x \pm iT^y$. At half-filling ($N = L$), $T^z = 0$.

[2] At half-filling the model also possesses the particle-hole symmetry $c_{i\sigma} \to (-1)^i c^{\dagger}_{i\sigma}$, equivalent to $T^z_i \to -T^z_i$, which yields no further compression when the full charge SU(2) is already enforced. The open boundary conditions (OBC) reduce translational symmetry to spatial inversion; while this could in principle be exploited, it offers no practical advantage for MPS-based codes, which are already highly efficient under OBC.

[3] The symmetry acts as the identity on $\mathbb{D}_{n,j}$; all variational degrees of freedom reside there.

symmetric bond dimension $\chi_{\mathrm{SU}(2)}$ is the truncation parameter we impose in our implementation. The *maximum* degeneracy $d^{\max}_{\mathrm{SU}(2)}$ most directly governs computational cost: working in the irrep basis reduces the SVD cost from $\mathcal{O}(\chi^3)$ to $\mathcal{O}((d^{\max}_{\mathrm{SU}(2)})^3)$. In practice we find $\chi \approx 2.4\,\chi_{\mathrm{SU}(2)}$. For $\mathrm{U}(1) \times \mathrm{U}(1)$ symmetry, $\chi = \chi_{\mathrm{U}(1)}$. Throughout this work, all quoted bond dimensions refer to χ.

S2.2 Adaptive TDVP algorithm

The time-dependent variational principle (*7, 8*) (TDVP) is the leading method for simulating the time evolution of 1D quantum systems beyond the reach of exact diagonalization. On a lattice with open boundary conditions, an MPS with bond dimension χ approximates the many-body wavefunction as

$$|\psi\rangle = \sum_{\{s_i\}} A_1^{s_1} A_2^{s_2} \cdots A_L^{s_L} |s_1 s_2 \cdots s_L\rangle, \tag{11}$$

where $s_i \in \{1, \ldots, d\}$ labels a basis state of the local d-dimensional Hilbert space, $A_i^{s_i} : \mathbb{V}^{[i-1]} \to \mathbb{V}^{[i]}$ are matrices acting on bond spaces $\{\mathbb{V}^{[i]}\}$ with $\dim(\mathbb{V}^{[i]}) = \chi_i$. The maximum value $\max_i\{\chi_i\}$ is the bond dimension of the MPS.

TDVP projects the Schrödinger equation onto the MPS tangent space and integrates the resulting equations of motion via DMRG-like sweeps over the lattice. At each sweep step, one or two MPS tensors are locally updated by exponentiating the effective Hamiltonian of the corresponding block via a Krylov-based matrix exponential; the Krylov subspace dimension is chosen adaptively (*35*), reducing unnecessary iterations at short effective time steps. The dominant cost per time step scales as $\mathcal{O}(L\chi^3 d)$, where d is the local Hilbert space dimension.

The key distinction between the 1-site and 2-site TDVP variants lies in how the bond dimension is controlled. In the 2-site algorithm, two adjacent tensors are merged and the bond between them is updated via SVD, allowing the bond dimension to grow adaptively

during the sweep. The 1-site algorithm, by contrast, keeps the bond dimension fixed, requiring it to be set large enough at initialisation to accommodate the entanglement at the end of the simulation. For quench dynamics — where entanglement grows rapidly — the 2-site algorithm is the more practical choice, since it avoids over-provisioning bond dimension early in the evolution. When symmetries are exploited (see next section), the 2-site algorithm also naturally provides a suitable distribution of the total bond dimension over the sparse blocks of the MPS tensors.

The Q-CTRL team employed 2-site TDVP throughout their simulation. We instead adopt an adaptive hybrid scheme: we begin with 2-site updates to allow the bond dimension to grow freely, then switch to 1-site updates once it has saturated. This yields a substantial runtime speedup — empirically factors of 4–10 for the subsequent time steps. The gain arises because the 2-site algorithm must perform an SVD of the merged two-site tensor (of size $d^2\chi^2$; $d = 4$ for the FHM) at every sweep step, an operation that becomes pure overhead once bond growth has ceased. Switching to 1-site updates, which propagate tensors of size $d\chi^2$, eliminates this cost entirely for the remainder of the simulation.

Since our implementation is independent of ITensor, we can apply this hybrid scheme natively without any manual partitioning of the time evolution. The Q-CTRL team did not report any such adaptation, and we assume their simulation used the 2-site algorithm throughout.

S2.3 GPU Acceleration

We implemented our $\mathrm{U}(1) \times \mathrm{SU}(2)$-symmetric TDVP algorithm in PyTorch with targeted low-level optimizations to leverage GPU acceleration (*24*). Similar approaches have been recently reported in quantum chemistry (*27–30*).

The dominant computational bottleneck in TDVP is the contraction of MPS tensors

with the matrix product operator (MPO) representation of the Hamiltonian H. More specifically, the dominant computational cost arises due to the updates of the left and right environments and the local Krylov exponentiation at each bond. These operations reduce to dense matrix multiplications involving tensors whose leading dimension scales as $\chi^2 dW$, where W is the MPO bond dimension ($W = 4$ for the FHM with $\mathrm{U}(1)\times\mathrm{SU}(2)$). At the large matrix sizes reached in our simulations, GPU GEMM[4] throughput substantially exceeds that of CPUs, making GPU execution a natural fit.

GPU-accelerating *symmetric* tensor network algorithms presents an additional challenge. The computational gain from symmetry arises by decomposing large tensors into block-diagonal form, replacing a single large matrix multiplication with a collection of smaller ones. On a GPU, however, this block structure can severely dilute arithmetic intensity: when individual blocks are small, the cost of data movement dominates over floating-point work, negating the GPU advantage—a limitation also noted in the ITensor library documentation (*25*). We mitigate this by *batching*: blocks of equal size are grouped and dispatched together as a single batched-GEMM call, replacing many small independent kernel launches with a shorter sequence of higher-occupancy operations. At large bond dimensions, the runtime is dominated by the contractions of the largest batches, which are substantially accelerated by GPUs.

At sufficiently large bond dimension, memory becomes the binding constraint on the GPU. We address this by reducing floating-point precision from `float64` to `float32`, which also yields a modest wall-clock speedup of 6–23% depending on bond dimension.

Floating-point precision in classical simulations must be commensurate with the accuracy of the hardware being benchmarked. The Q-CTRL quantum circuits are wide and deep, and the resulting noise floor of the QPU substantially exceeds the rounding

[4]The routine for GEneral Matrix Multiplications in the cuBLAS library.

errors introduced by single-precision (float32) arithmetic. Using double precision (float64) would therefore provide no meaningful improvement in benchmark fidelity while significantly increasing memory and compute costs. To validate this, we compared float32 and float64 simulations over a representative portion of the evolution and confirmed that all physically relevant observables agree to within our target accuracy, see Sect. S2.5. One potential concern with float32 is the accumulation of rounding errors over many time steps; we show explicitly that this does not occur here, and that single precision remains reliable throughout the full simulation window.

After all optimizations on a single GPU have been exhausted, one can still push the numerics by using multiple GPUs. In this case, we distributed the batches of matrix multiplications across the devices using a greedy load-balancing rule that aims to maximize the utilization of each device, while performing the SVDs on the CPU using 16 threads. Furthermore, only the active local tensors, environments, effective Hamiltonian data, and current Krylov vector are staged to the GPU devices to preserve memory, while the CPU acts as the storage device. Our largest simulation at $\chi \approx 62{,}000$ ($\epsilon_{\text{tol}} = 10^{-6}$, `float32`) took 16h 12m until $t = 7$. See Table S1 for runtimes of all our experiments.

S2.4 SVD truncation threshold

For a global quench, the entanglement entropy is believed to grow linearly $S(t) = a \cdot t$ (*36*), which means that the bond dimension should grow exponentially $\chi(t) \sim \exp(at)$. TDVP achieves this growth by doing 2-site updates, which increases the maximum possible number of states on the link, and then keeping the most relevant states using SVD.

An important hyperparameter is the compression tolerance, i.e. the threshold for the sum of discarded singular values ("truncated weight"), which regulates the growth rate. Setting it too large will not faithfully follow the state, while setting it too small will lead

to unnecessarily expensive computations. In Fig. S1, we vary the compression tolerance across several orders of magnitude without capping the bond dimension and propagating until the numerical resources are exhausted, while looking at the observable $\langle n_{46\uparrow} \rangle$. We find that for the given problem, even a tolerance of 10^{-4} is sufficient to capture the observable at least until $t \sim 5$, and this is the value we use in the plots of the main text.

Note that we would still like to propagate further with a capped bond dimension beyond this. Even though the exponential growth of χ cannot be followed further, it does not mean that the results immediately become invalid. To get a sense of the errors in this case, we compare the results with $\epsilon_{\text{tol}} = 10^{-4}, 10^{-5}$ to the most accurate result at $\epsilon_{\text{tol}} = 10^{-6}$ in Fig. S2 and find that the error in the observable remains at most of order $O(10^{-2})$.

S2.5 Float32 vs. float64 validation

The noise floor of the Q-CTRL quantum circuits substantially exceeds the rounding errors of `float32` arithmetic, so single precision suffices for benchmarking purposes. Figure S3 compares `float32` and `float64` evolutions; the absolute deviation in $\langle n_{46\uparrow} \rangle$ remains below 10^{-3} throughout. Using `float32` also yields a modest 6–23% wall-clock speedup and halves GPU memory consumption, enabling the largest bond dimensions.

S3 Density profile comparison

Figure S4 shows the full density profile computed with $\mathrm{U}(1) \times \mathrm{U}(1)$ symmetry at $\chi = 4096$ and $\epsilon_{\text{tol}} = 10^{-4}$ — a comparison absent from the Q-CTRL paper (*1*). The profiles deviate visibly at late times, confirming that this bond dimension is insufficient for convergence. Switching to $\mathrm{U}(1) \times \mathrm{SU}(2)$ symmetry, convergence is achieved at $\chi \approx 30{,}000$ (Fig. S5).

S4 Supplementary Figures and Tables

ϵ_{tol}	Symmetry	Prec.	$\chi_{\text{SU(2)}}$	χ	N_{GPU}	$t = 6$	$t = 7$
10^{-4}	U(1)×U(1)	fp64	—	4 096	1	3h 27m	—
	U(1)×SU(2)	fp64	2 048	4 880	1	1h 51m	—
	U(1)×SU(2)	fp32	2 048	4 880	1	1h 40m	—
	U(1)×SU(2)	fp64	4 096	10 000	1	2h 30m	2h 42m
	U(1)×SU(2)	fp64	8 192	20 000	1	3h 33m	3h 51m
	U(1)×SU(2)	fp32	12 288	30 000	1	4h 06m	4h 27m
	U(1)×SU(2)	fp32	16 384	41 000	2	5h 31m	8h 20m
	U(1)×SU(2)	fp32	24 576	62 000	4	5h 21m	13h 57m
10^{-5}	U(1)×U(1)	fp64	—	4 096	1	3h 51m	—
	U(1)×SU(2)	fp64	2 048	4 880	1	2h 15m	—
	U(1)×SU(2)	fp32	2 048	4 880	1	2h 49m	—
	U(1)×SU(2)	fp64	4 096	10 000	1	2h 53m	3h 06m
	U(1)×SU(2)	fp64	8 192	20 000	1	3h 29m	3h 49m
	U(1)×SU(2)	fp32	12 288	30 000	1	5h 26m	5h 48m
	U(1)×SU(2)	fp32	16 384	41 000	2	7h 13m	8h 11m
	U(1)×SU(2)	fp32	24 576	62 000	4	13h 33m	15h 40m
10^{-6}	U(1)×U(1)	fp64	—	4 096	1	3h 59m	—
	U(1)×SU(2)	fp64	2 048	4 880	1	2h 02m	—
	U(1)×SU(2)	fp64	4 096	10 000	1	2h 49m	3h 02m
	U(1)×SU(2)	fp64	8 192	20 000	1	3h 32m	3h 53m
	U(1)×SU(2)	fp32	12 288	30 000	1	4h 28m	4h 51m
	U(1)×SU(2)	fp32	16 384	41 000	2	7h 24m	8h 21m
	U(1)×SU(2)	fp32	24 576	62 000	4	14h 08m	16h 12m

Table S1: Wall-clock runtime to reach $t = 6$ and $t = 7$ as a function of convergence tolerance ϵ_{tol} and bond dimension. Runtimes are non-monotonic because the algorithm adaptively switches from 2-site to 1-site TDVP once the bond dimension saturates.

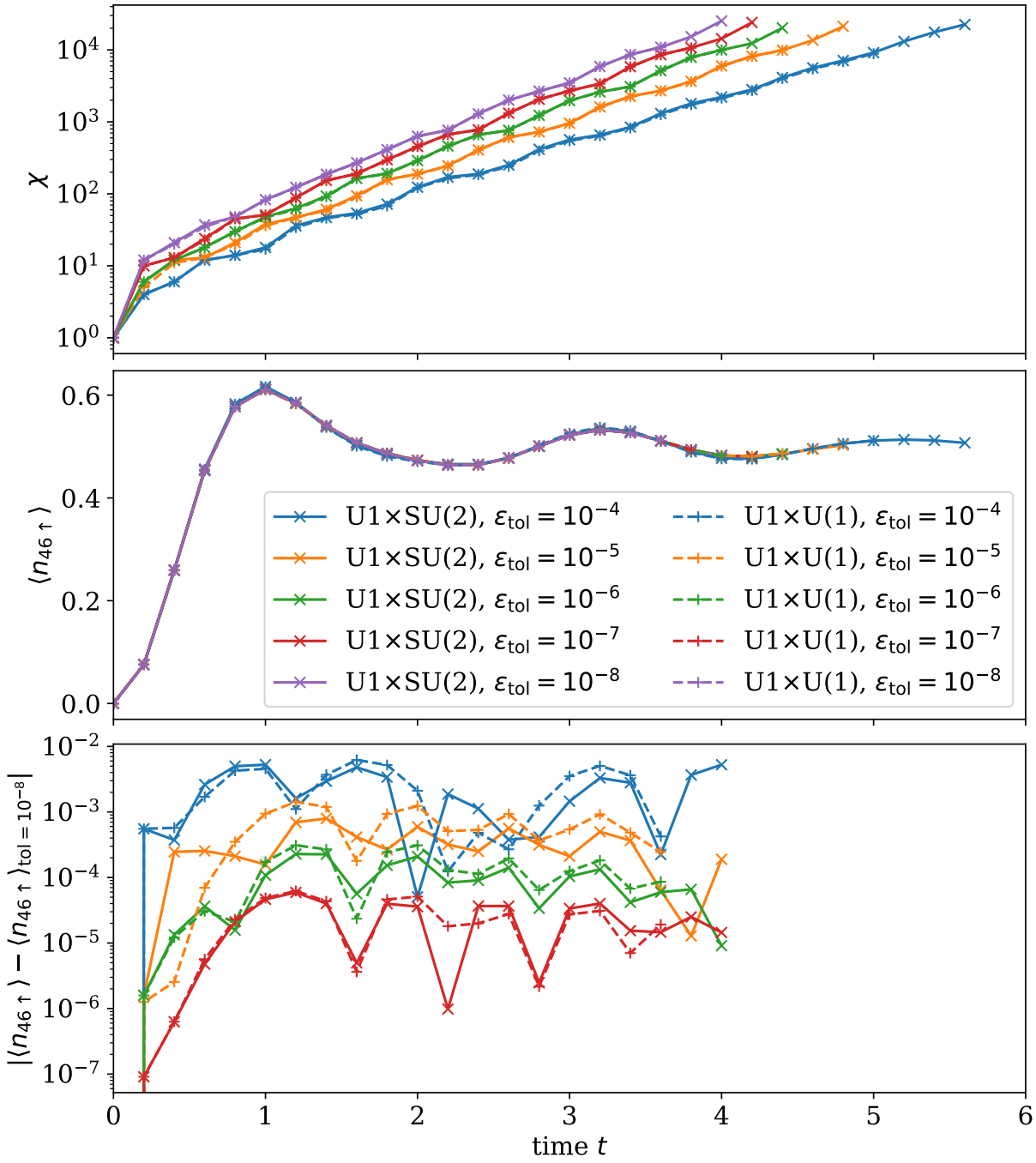

Figure S1: SVD tolerance analysis with unrestricted bond dimension. Top: exponential $\chi(t)$ growth for different ϵ_{tol}. Middle: the observable $\langle n_{46\uparrow} \rangle$ is nearly identical across tolerances. Bottom: deviation from the most accurate result ($\epsilon_{\mathrm{tol}} = 10^{-8}$).

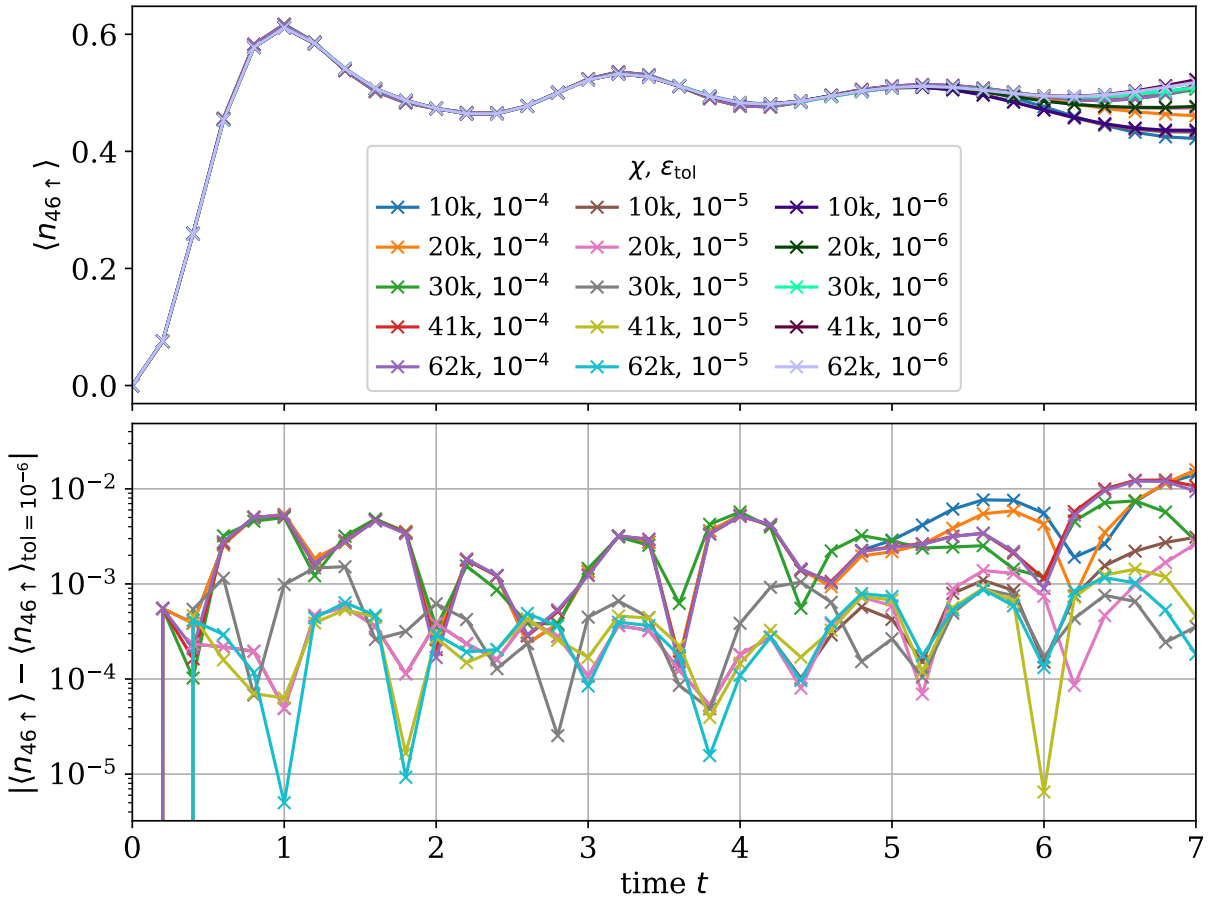

Figure S2: Tolerance comparison with capped bond dimension and the adaptive 1-site/2-site switch. Top: $\langle n_{46\uparrow} \rangle$ for each (χ, ϵ_{tol}) combination. Bottom: deviation from the $\epsilon_{\text{tol}} = 10^{-6}$ reference.

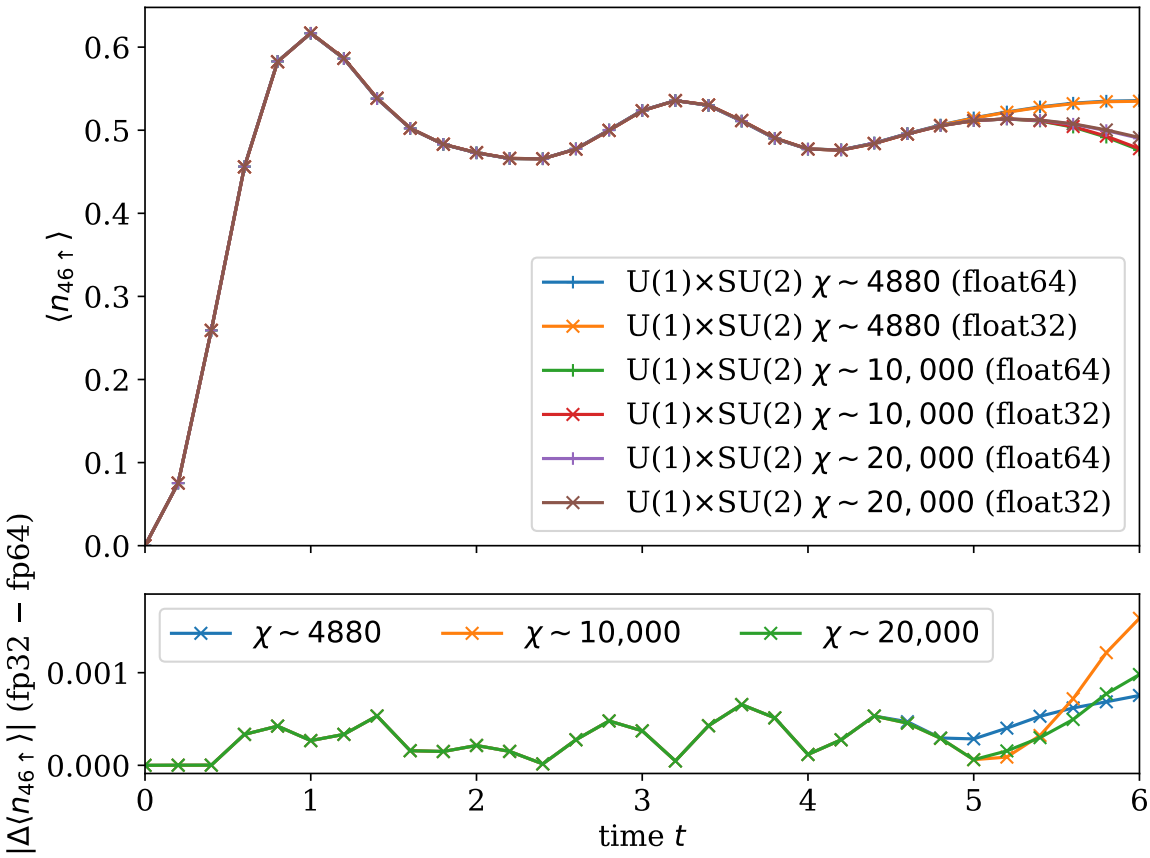

Figure S3: Float32 vs. float64 comparison at $\epsilon_{\text{tol}} = 10^{-4}$. Top: $\langle n_{46\uparrow} \rangle$ for both precisions. Bottom: absolute difference, remaining $O(10^{-3})$ or smaller throughout.

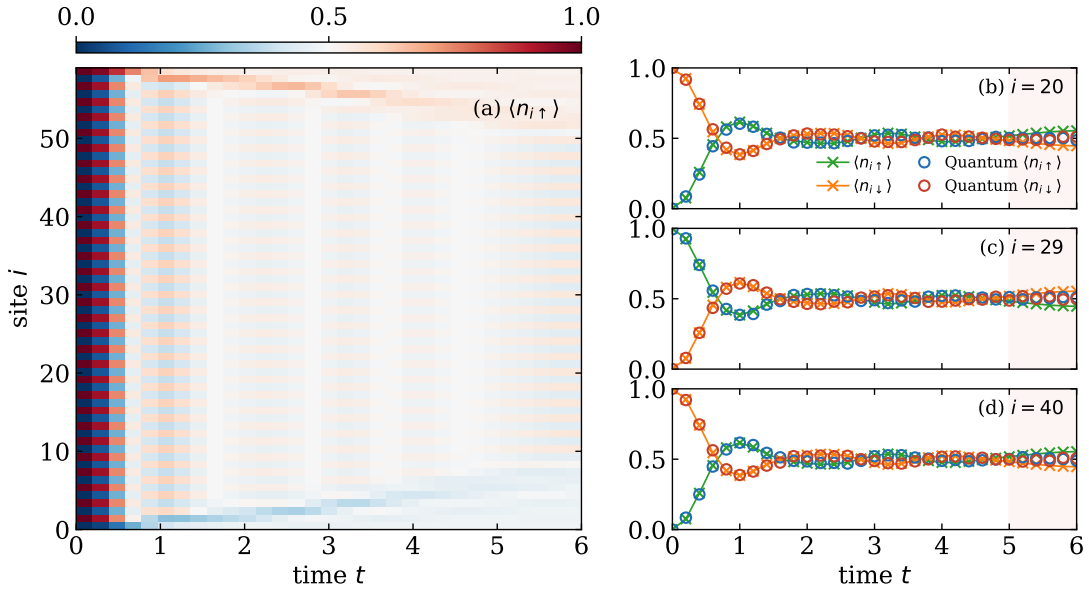

Figure S4: Density heatmap as in Fig. 2 but using $\mathrm{U}(1) \times \mathrm{U}(1)$ symmetry at $\chi = 4096$, $\epsilon_{\mathrm{tol}} = 10^{-4}$. Visible deviations at late times confirm that this bond dimension is insufficient to benchmark the quantum results (area shaded red).

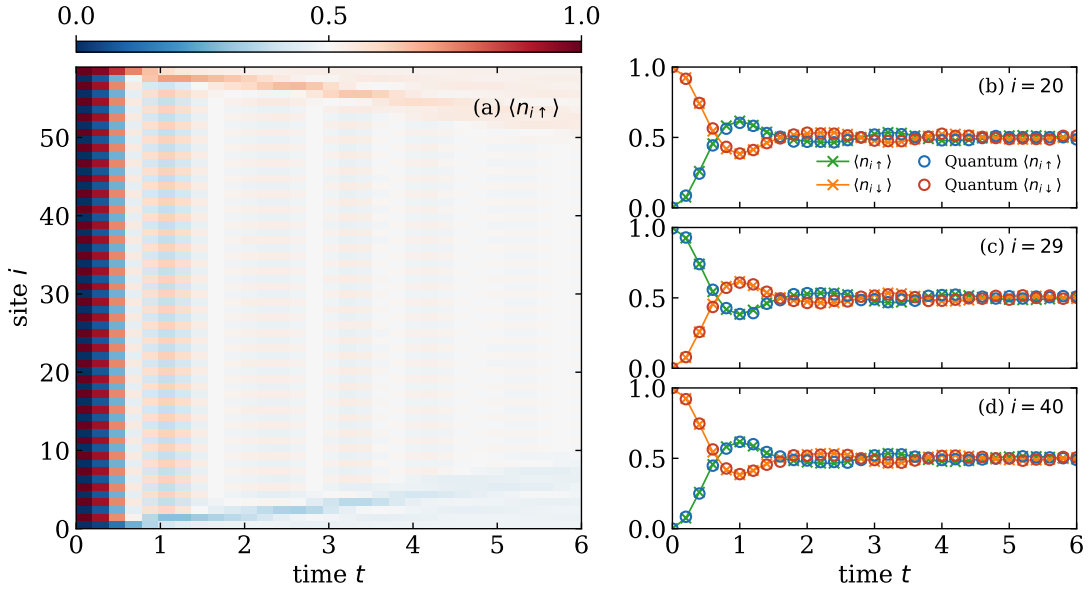

Figure S5: Density heatmap as in Fig. 2, but computed with $\mathrm{U}(1) \times \mathrm{SU}(2)$ symmetry at $\chi \approx 30{,}000$ and $\epsilon_{\mathrm{tol}} = 10^{-4}$. These parameters are sufficient for convergence up to $t = 6$.

Table S2: Irrep degeneracies $d_{n,j}$ for the 32 symmetry sectors present at $t = 6$ in our U(1) $\times$ SU(2) TDVP evolution at $\chi_{\mathrm{SU(2)}} = 12{,}288$ ($\chi \approx 30{,}000$), for the left bond of the MPS tensor at site 30.

n	j	$d_{n,j}$	n	j	$d_{n,j}$
-6	0	8	0	0	1097
-6	1	1	0	1	1387
-5	$\frac{1}{2}$	86	0	2	287
-5	$\frac{3}{2}$	13	0	3	8
-4	0	241	1	$\frac{1}{2}$	1157
-4	1	233	1	$\frac{3}{2}$	494
-4	2	19	1	$\frac{5}{2}$	42
-3	$\frac{1}{2}$	799	2	0	382
-3	$\frac{3}{2}$	307	2	1	421
-3	$\frac{5}{2}$	10	2	2	67
-2	0	920	3	$\frac{1}{2}$	178
-2	1	1135	3	$\frac{3}{2}$	58
-2	2	213	4	0	35
-1	$\frac{1}{2}$	1735	4	1	29
-1	$\frac{3}{2}$	837	5	$\frac{1}{2}$	8
-1	$\frac{5}{2}$	80	6	0	1